

# Reconstruct Anything Model: a lightweight foundation model for computational imaging

Matthieu Terris  
Université Paris-Saclay, Inria, CEA  
Palaiseau, 91120, France

Samuel Hurault  
ENS Paris, PSL, CNRS  
Paris, 75005, France

Maxime Song  
CNRS UAR 851, Université Paris-Saclay  
Orsay, 91403, France

Julián Tachella  
ENSL, CNRS UMR 5672  
Lyon, 69342, France

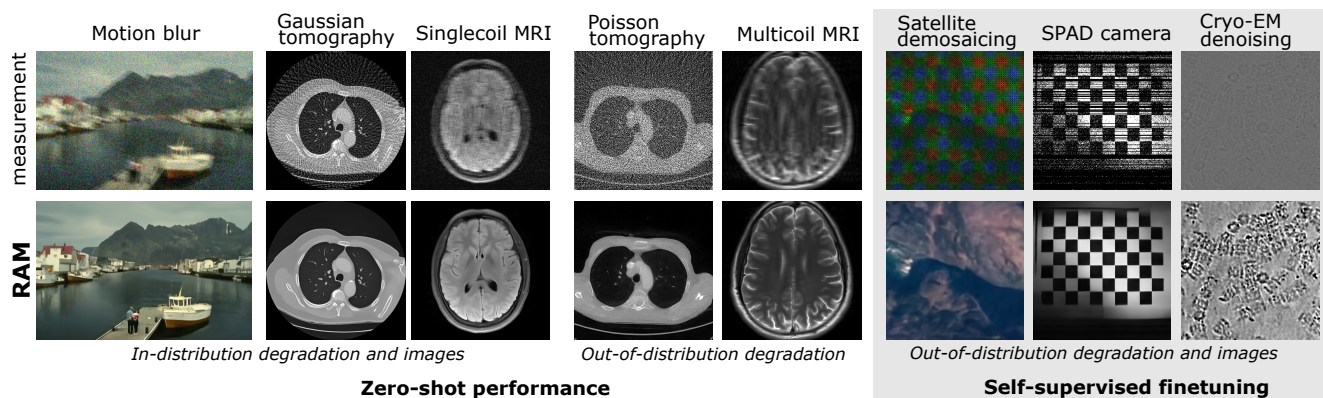


Figure 1. The RAM model can solve a wide variety of inverse problems, from medical imaging to microscopy and low-photon imaging, obtaining state-of-the-art zero-shot performance in imaging problems and datasets in or close to the training distribution. RAM can also be finetuned in a self-supervised way (without any ground truth references) for out-of-distribution images and/or imaging problems.

## Abstract

Most existing learning-based methods for solving imaging inverse problems can be roughly divided into two classes: iterative algorithms, such as plug-and-play and diffusion methods, that leverage pretrained denoisers, and unrolled architectures that are trained end-to-end for specific imaging problems. Iterative methods in the first class are computationally costly and often provide suboptimal reconstruction performance, whereas unrolled architectures are generally specific to a single inverse problem and require expensive training. In this work, we propose a novel non-iterative, lightweight architecture that incorporates knowledge about the forward operator (acquisition physics and noise parameters) without relying on unrolling. Our model is trained to solve a wide range of inverse problems beyond denoising, including deblurring, magnetic resonance imaging, computed tomography, inpainting, and super-resolution. The proposed model can be easily adapted to unseen inverse problems or datasets with a few fine-tuning steps (up to a few images) in a self-supervised way, without ground-truth references. Throughout a series of experiments, we demonstrate state-of-the-art performance from medical imaging to low-photon imaging and microscopy.

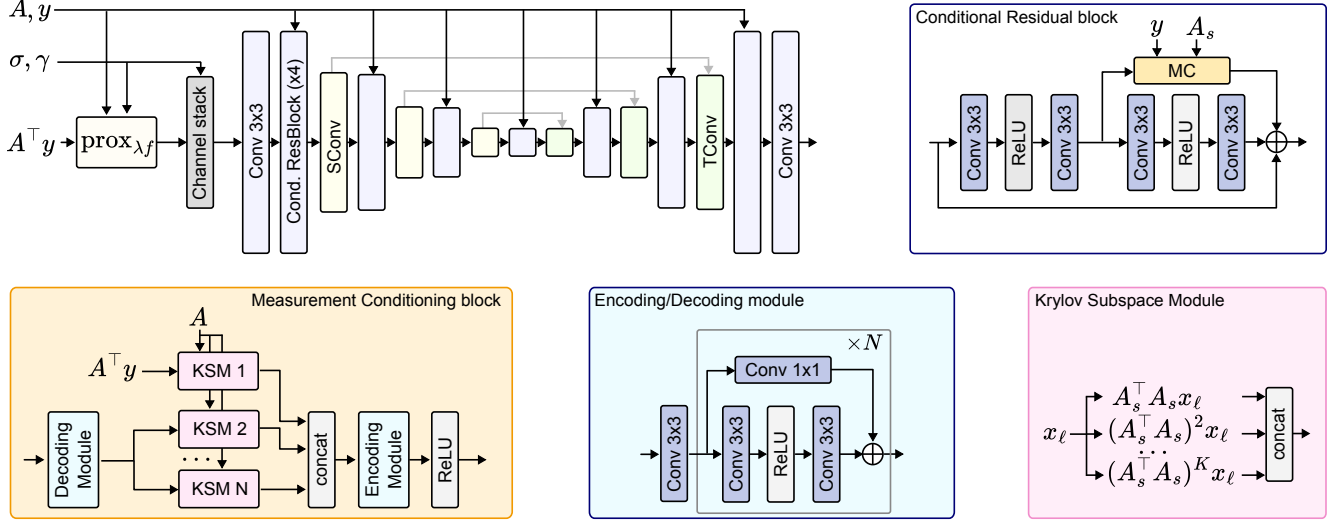


Figure 2. **Proposed architecture for solving non-blind imaging inverse problems.** *Top row:* The architecture builds upon a DRUNet backbone, originally designed with convolutional and residual blocks, but is enhanced to integrate knowledge about the measurement operator  $A$  and measurements  $\mathbf{y}$ . *Bottom row:* At each scale, feature maps are decoded into the image domain, processed through a Krylov subspace module (KSM), and then re-encoded. The encoding/decoding module consists of a simple residual convolutional block. The KSM blocks concatenate power iterations of the scaled measurement operator  $A_s^\top A_s$ , enabling efficient and adaptable processing for a wide range of inverse problems.

## 1. Introduction

Computational imaging problems are ubiquitous in applications ranging from demosaicing in computational photography to Magnetic Resonance Imaging (MRI). In this work, we focus on linear inverse problems of the form

$$\mathbf{y} \sim p(\mathbf{y} | A\mathbf{x}), \quad (1)$$

where  $\mathbf{x} \in \mathbb{R}^n$  is the image to recover,  $\mathbf{y} \in \mathbb{R}^m$  are measurements,  $A: \mathbb{R}^n \rightarrow \mathbb{R}^m$  is an operator, usually assumed to be linear (e.g. some blurring or masking operation) and  $p$  is the noise distribution, which can typically be Gaussian and/or Poisson noise. We stress that we mostly consider non-blind problems, i.e. we assume that both the operator  $A$  and the parameters of the noise model  $p$  are known.

The most common approach to solving the inverse problem (1) is to employ an iterative algorithm to minimize an objective function of the form

$$\arg\min_{\mathbf{x}} \frac{1}{2} \|A\mathbf{x} - \mathbf{y}\|_2^2 + g(\mathbf{x}), \quad (2)$$

where  $g$  encodes prior knowledge about the data. Traditionally, handcrafted priors, such as total variation [49] or wavelet sparsity [35] have been employed to regularize the solution. However, recent advances have highlighted the effectiveness of learned priors, particularly deep denoising neural networks, which have been successfully integrated into iterative reconstruction methods. These include Plug-and-Play (PnP) algorithms [21, 24, 42, 60], and the more recent diffusion models-based methods [12, 13, 73]. The advantage of these approaches is that a single model trained only for denoising can be used to solve a large set of image restoration tasks. However, these methods come with several major drawbacks. First, their iterative nature often leads to slow reconstructions, making them less practical for time-sensitive applications. Second, it has been observed [10, 37, 59] that using a denoiser as an image prior can introduce undesired blur artifacts. Third, the performance of these approaches is highly dependent on the dataset used to train the denoiser, which strongly limits their applicability in scenarios where only a small amount of training data is available, such as in medical imaging or microscopy [7].

Another common strategy for solving (1) is to train an end-to-end deep neural network specifically for the given task. In low-level vision applications such as single-image super-resolution and image denoising, architectures are often derived empirically, with UNet-based models emerging as a standard choice [69, 70]. However, in computational imaging tasks (e.g. MRI, computed tomography, astronomical imaging), unrolled optimization-inspired architectures are typically preferred due to their ability to incorporate the measurement operator and observed data [1, 18, 44]. Despite this, the architectural choices

that perform best in simpler tasks such as denoising often differ significantly from those used in unrolling, and it remains unclear whether this approach is necessary—or even optimal—for neural network design. In particular, empirical results [64, 65, 69, 70] suggest that effective architectures need not strictly adhere to optimization-derived operations. In both cases, however, even minor architectural modifications—such as adjusting the number of input and output channels—often require full model retraining. This reduces adaptability across datasets and inverse problems with similar statistical properties, such as transitioning from grayscale to color images or handling complex multi-channel representations [32].

In this work, we propose a novel neural network architecture for solving (1), building on the DRUNet convolutional neural network [69]. Our key modification introduces a conditioning mechanism that integrates the acquisition physics  $(A, p)$  through multigrid Krylov iterations. We train a single backbone model across multiple imaging tasks simultaneously ranging from image deblurring to MRI, handling datasets with grayscale, color, and complex images, corrupted by both Gaussian and Poisson noise. As a result, our architecture supports grayscale (1 channel), complex-valued (2 channels), and color images (3 channels), with only the output heads differing to accommodate specific channel numbers. Beyond its strong zero-shot performance, we demonstrate that the model can be efficiently fine-tuned in a self-supervised way on real measurement data.

## 2. Related works

**Implicit denoising priors** Diffusion [12, 27, 53] and Plug-and-Play (PnP) [45, 46, 60, 69] algorithms make use of a denoising neural network trained on a given dataset of interest. This denoiser approximates the score of the underlying data distribution [61], thus providing a way to implicitly regularize (2) [13]. This denoising prior can thus be used to solve any inverse problem beyond its original training denoising task. In this context, the architecture of choice for denoising tasks is the UNet [28, 47, 53]. In [69], the authors propose to use a bias-free residual UNet, called *DRUNet*. This property endows the model with scaling equivariance properties, enabling the model to generalize beyond noise levels seen during training [20, 38].

**End-to-end architectures** Several architectures have imposed themselves as cornerstone in the low-level vision community. Early breakthroughs include the UNet [25, 48] and deep residual convolutional networks [66, 67, 71]. More recently, architectures incorporating attention mechanisms have surpassed previous state-of-the-art models [32, 64, 70]. A clear trend has emerged, where empirical approaches drive the discovery of task-specific architectures trained and tested on the same distribution. Notable recent developments include transformer-based models, particularly in single-image super-resolution [32, 64], and, more recently, state-space models [16]. Despite these advances, the UNet remains a key backbone for many state-of-the-art methods, see e.g. [64, 70], incorporating transformer blocks on UNet-like architectures.

**Unrolled architectures** To better condition on the acquisition physics, unrolled networks introduce learnable neural modules (e.g. convolutional layers) within the iterations of an optimization algorithm solving (2). Several architectures have become standard in this framework, including the primal-dual network (PDNet) [1], the variational network (VarNet) [18], and the NC-PDNet [44] for non-Cartesian MRI. More recently, [68] proposed an unrolled version of the plug-and-play DPIP algorithm and [9], an unrolled interior point algorithm using the IRCNN architecture [67]. These models have been particularly successful in medical imaging and other computational imaging domains, such as astronomical imaging [3]. For applications in natural image processing, see [9, 51, 68]. However, these models are typically trained on a single or limited set of tasks with limited variations. Moreover, there is a significant discrepancy between the overall architecture of these unrolled models and the highly effective architectures employed by the previously discussed end-to-end approaches.

**Conditioning strategies** Building on advances in conditional generative modeling (e.g. text-to-image tasks), the diffusion literature has introduced modifications to UNet architectures to incorporate conditioning signals, such as textual descriptions or class embeddings. In the seminal work of [47], the authors introduced cross-attention to condition a denoising UNet on text, a technique now widely adopted in diffusion-based architectures [50]. More recently, the ControlNet [34] approach has been proposed to incorporate external control or conditioning into the backbone denoiser of diffusion-based models. Furthermore, all diffusion-based architectures condition the model on the noise level in a non scale equivariant way, unlike [28, 69].

**Self-supervised learning** In many scientific and medical imaging problems, obtaining ground-truth data for supervised training is expensive or even impossible [7]. Recent advances in self-supervised learning allow training a network from

measurement data alone [6, 11, 56, 62]. Here we show that self-supervision is highly effective for finetuning a foundation model with few or no ground-truth references.

### 3. Proposed approach

#### 3.1. Proposed architecture

The proposed architecture is derived from the celebrated DRUNet [69]. We detail below the various modifications that we bring to the network in order to handle general inverse problems.

**Proximal estimation module** In order to solve (1) in a general way for all inverse problems, a first step is to map  $\mathbf{y}$  onto the appropriate image domain. Several approaches are used in the literature, using either  $A^\dagger \mathbf{y}$  as the input of the network or  $A^\top \mathbf{y}$ . The first approach shows the advantage of inverting the ill-conditioning of  $A$  but is extremely sensitive to noise. In noisy settings, the latter approach is often chosen, at the cost of significant blurring of the input. Instead, setting  $f(\mathbf{x}, \mathbf{y}) = \frac{1}{2} \|A\mathbf{x} - \mathbf{y}\|_2^2$ , our first estimation step consists in a proximal step

$$\text{prox}_{\lambda f}(A^\top \mathbf{y}) = \underset{\mathbf{u}}{\text{argmin}} \lambda \|A\mathbf{u} - \mathbf{y}\|^2 + \|\mathbf{u} - A^\top \mathbf{y}\|^2, \quad (3)$$

where  $\lambda > 0$  is a regularization parameter. (3) can be seen as a middle-ground between  $A^\top \mathbf{y}$  (when  $\lambda$  is low) and  $A^\dagger \mathbf{y}$  (when  $\lambda$  is large). We set  $\lambda$  proportional to the input SNR as  $\lambda = \sigma\eta / \|\mathbf{y}\|_1$  where  $\sigma$  is the Gaussian noise level and  $\eta$  is a learnable parameter.

**Krylov subspace module** Given an intermediate estimate of the image  $\mathbf{x}^\ell$ , unrolled network architectures condition on the acquisition physics  $A$  via a gradient step, i.e.

$$\mathbf{x}^{\ell+1} = \mathbf{x}^\ell - \lambda A^\top (A\mathbf{x}^\ell - \mathbf{y})$$

or a proximal gradient step, i.e.

$$\mathbf{x}^{\ell+1} = \underset{\mathbf{u}}{\text{argmin}} \lambda \|A\mathbf{u} - \mathbf{y}\|^2 + \|\mathbf{u} - \mathbf{x}^\ell\|^2.$$

The minimization problem in the proximal gradient step is commonly solved using an iterative conjugate gradient solver. Since conjugate gradient is a Krylov subspace method [29, 30, 40], the solver provides a solution in  $K$  iterations that lies on the span of  $\{(\lambda I + A^\top A)^k (A^\top \mathbf{y} + \lambda \mathbf{x}^\ell)\}_{k=0}^K$ , and both steps can be written as

$$\mathbf{x}^{\ell+1} = \sum_{k=0}^K \alpha_k (A^\top A)^k \mathbf{x}^\ell + \beta_k (A^\top A)^k A^\top \mathbf{y} \quad (4)$$

for some scalar coefficients  $\{(\alpha_k, \beta_k)\}_{k=1}^K$ .

Thus, we propose to condition on  $A$  using a Krylov Subspace Module (KSM), which learns the linear combination coefficients  $\{(\alpha_k, \beta_k)\}_{k=1}^K$ . Given an intermediate latent representation, a decoding module first maps the features onto the image domain using a convolution layer. Then, it stacks  $\left\{ \left( (A^\top A)^k \mathbf{x}^\ell, (A^\top A)^k A^\top \mathbf{y} \right) \right\}_{k=1}^K$  along channels and combines them through a  $3 \times 3$  convolution. The output is finally added to the latent space via a convolutional encoding module, see Figures 2 and 3 for more details.

**Multiscale operator conditioning** For a fixed number of measurements  $m$ , the finer the grid (i.e. larger  $n$ ), the more ill-posed the inverse problem becomes, as the dimension of the nullspace of  $A$  is lower bounded by  $n - m$ . Thus, inspired by multigrid methods [17], we propose to condition our architecture on forward operators defined on coarse grids as:

$$A_s = AU_s \quad (5)$$

where  $U_s : \mathbb{R}^{\frac{n}{4^s}} \rightarrow \mathbb{R}^m$  is a  $s \times$  upsampling operator with a Kaiser-windowed sinc antialias filter [26]. Figure 3 shows how the linear pseudoinverse is unstable on a fine grid and stable on a coarse grid. We normalize all operators to have unit norm at each scale, i.e.  $\|A_s\|_2 = 1$  for all  $s$ . Moreover, for many inverse problems, we can develop efficient implementations of  $A_s^\top A_s \in \mathbb{R}^{\frac{n}{4^s} \times \frac{n}{4^s}}$  and  $A_s^\top \mathbf{y} \in \mathbb{R}^{\frac{n}{4^s}}$  which can be computed fully on the coarse grid, avoiding any expensive fine scale computations. For example, if  $A$  represents a blur or an inpainting operation, we can simply downscale the kernel or the inpainting mask respectively.

**Noise conditioning & biases** Similarly to [69], conditioning on the noise level is performed via a stacking of constant maps on the channel dimension. While a single noise map was added for Gaussian denoising in [69], we propose to have two noise level maps to enable our architecture to account for Poisson-Gaussian noise of the form

$$\mathbf{y} = \gamma \mathbf{z} + \sigma \mathbf{n}, \quad (6)$$

where  $\gamma \geq 0$  is the gain factor<sup>1</sup> associated to the Poisson noise  $\mathbf{z} \sim \mathcal{P}(\mathbf{x}/\gamma)$ , and  $\sigma \geq 0$  is the standard deviation of the Gaussian component of the noise, with  $\mathbf{n} \sim \mathcal{N}(\mathbf{0}, I)$ . In turn, we stack constant maps filled with values  $\sigma$  and  $\gamma$  to the channels of the input data. All biases are removed from our architecture to ensure a scale equivariance property with respect to both the  $\sigma$  and  $\gamma$  components, enabling better generalization to unseen noise levels [38, 69].

**Shared layers between imaging modalities** The architectural modifications required to accommodate to inputs with varying channel numbers (color, grayscale, or complex images) affect only a small fraction of the model’s total parameters. Specifically, only the first (input) and last (output) convolutional layers of the DRUNet, as well as the encoding and decoding blocks within the KSM modules, are adjusted to account for varying channel numbers. All other weights of the model are shared across modalities.

### 3.2. Training

We train our network *simultaneously* on  $G$  computational imaging tasks, spanning image restoration (deblurring, inpainting, Poisson-Gaussian denoising in both color and grayscale), single-coil MRI, CT, and others (see Appendix for a complete list), leveraging the `deepinv` library that implements all the operators in a common framework [57]. Each task  $g$  is associated with a dataset  $\mathcal{D}_g = \{\mathbf{x}_{i,g}\}_{i=1}^{N_g}$ : LSDIR [31] for tasks involving natural images, LIDC-IDRI for CT images [5], and the fastMRI brain-multicoil dataset for MRI [65].

Furthermore, each task  $g$  can be framed as an inverse problem (1), where the measurements using the Poisson Gaussian noise model in (6) with varying gain  $\gamma \geq 0$  and standard deviation  $\sigma \geq 0$ . Our model is trained in a supervised fashion to minimize the following task-wise loss:

$$\mathcal{L}_g(\theta, \mathbf{x}_{i,g}) = \mathbb{E}_{(\sigma_g, \gamma_g)} \mathbb{E}_{\mathbf{y} | \mathbf{x}_{i,g}} \omega_g \| R_\theta(\mathbf{y}, A_g, \sigma_g, \gamma_g) - \mathbf{x}_{i,g} \|_1$$

where  $R_\theta$  is the model to be trained,  $A_g$  is the measurement operator of task  $g$ , and  $(\sigma, \gamma)$  are the noise parameters sampled from a distribution  $p(\sigma, \gamma)$ . We choose the  $\ell_1$  over the standard  $\ell_2$  loss as it was empirically observed to obtain better test performance [72]. We consider a weighting parameter  $\omega_g = \|A_g^T \mathbf{y}\| / \sigma_g$  to ensure the training loss is balanced across different noise levels and tasks. The final training loss is obtained by summing over all tasks:

$$\mathcal{L}(\theta) = \sum_{g=1}^G \sum_{i=1}^{N_g} \mathcal{L}_g(\theta, \mathbf{x}_{i,g}). \quad (7)$$

This formulation allows the network to generalize across multiple imaging modalities by learning from diverse measurement operators and noise distributions.

For each of the training inverse problems, we extract a random image patch  $\mathbf{x}_{i,g}$  of size  $(C, 128, 128)$  with  $C \in \{1, 2, 3\}$  to which we apply the measurement  $A_g$ . We use the pretrained weights of the DRUNet denoiser [69] to initialize our model. The model is trained with a batch of size 16 per inverse problem considered and for a total of 200k steps. We use the Adam optimizer with learning rate  $10^{-4}$  which is divided by 10 after 180k steps.

## 4. Self-supervised finetuning

Many real computational imaging applications are associated with a forward model that has not been seen during training, and have limited or no ground-truth reference data [7]. In such cases, the RAM model can be finetuned using measurement data alone, leveraging some of the recent advances in self-supervised learning for inverse problems [11, 15, 19, 23, 55, 58].

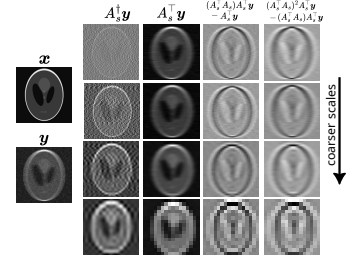


Figure 3. **Multiscale conditioning.** Estimating the underlying image (here motion blur) is easier on a coarser grid than a fine grid, as the forward operator is more ill-posed in the latter case.

<sup>1</sup>We use the convention that for  $\gamma = 0$  the noise model becomes purely Gaussian.

Table 1. Results on Motion Blur (left) and Gaussian Blur (right). Best result in red - second best in blue.

Method	Params	CBSD68 [36]			Urban100 [22]			Div2K [4]			CBSD68 [36]			Urban100 [22]			Div2K [4]		
		Easy	Med.	Hard	Easy	Med.	Hard	Easy	Med.	Hard	Easy	Med.	Hard	Easy	Med.	Hard	Easy	Med.	Hard
PDNet		30.54	26.84	24.62	28.36	25.22	22.67	32.61	28.81	26.32	29.88	25.26	22.55	27.85	22.81	19.90	32.01	27.29	24.03
Restormer		30.96	26.99	25.00	28.21	24.75	23.13	28.56	25.75	25.00	31.68	25.93	23.19	29.07	24.00	20.99	30.01	27.20	25.00
DPIR	32M	33.45	26.53	24.42	<b>34.39</b>	28.12	24.38	<b>36.32</b>	29.97	27.16	<b>32.10</b>	25.70	22.73	<b>32.53</b>	23.78	20.38	<b>35.23</b>	28.14	24.71
uDPIR-tied	32M	<b>33.78</b>	<b>28.20</b>	<b>25.61</b>	33.07	<b>28.73</b>	<b>25.42</b>	35.79	<b>30.76</b>	<b>27.91</b>	31.90	<b>26.10</b>	<b>23.41</b>	30.47	24.31	<b>21.05</b>	<b>34.63</b>	<b>28.45</b>	<b>25.20</b>
uDPIR-untied	256M	33.64	27.90	25.54	32.72	28.14	25.28	35.38	30.17	27.77	31.86	26.03	23.38	30.26	<b>24.32</b>	21.04	34.47	28.37	<b>25.23</b>
RAM	36M	<b>34.04</b>	<b>28.22</b>	<b>25.64</b>	<b>33.61</b>	<b>28.63</b>	<b>25.30</b>	<b>36.18</b>	<b>30.72</b>	<b>27.89</b>	<b>32.59</b>	<b>26.19</b>	<b>23.42</b>	<b>31.78</b>	<b>24.65</b>	<b>21.12</b>	<b>35.23</b>	<b>28.56</b>	25.16

In particular, we can finetune our pretrained RAM model with a loss that only requires a dataset of noisy and/or incomplete observations  $\{\mathbf{y}_1, \dots, \mathbf{y}_N\}$ :

$$\mathcal{L}(\theta) = \sum_{i=1}^N \mathcal{L}_{\text{MC}}(\theta, \mathbf{y}_i) + \omega \mathcal{L}_{\text{NULL}}(\theta, \mathbf{y}_i), \quad (8)$$

where the first term enforces measurement consistency  $A\hat{\mathbf{x}} \approx A\mathbf{x}$  while taking care of the noise [58], whereas the second term handles the lack of information in the nullspace of  $A$  [56], and  $\omega > 0$  is a trade-off parameter.

**Measurement consistency**  $\mathcal{L}_{\text{MC}}$  can be selected based on prior knowledge of the noise distribution [58]. If the noise distribution is known exactly, Stein’s Unbiased Risk Estimate (SURE) [54] is used. For the case of Gaussian noise of level  $\sigma$ , SURE is defined<sup>2</sup> as

$$\mathcal{L}_{\text{SURE}}(\theta, \mathbf{y}_i) = \|A_i \text{R}_\theta(\mathbf{y}_i, A_i) - \mathbf{y}_i\|_2^2 + 2\sigma_i^2 \text{div}(A_i \circ \text{R}_\theta)(\mathbf{y}_i, A_i)$$

where the divergence is approximated using a Monte Carlo method [43]. Extensions of SURE to unknown  $\sigma$  [58] and other noise distributions exist [39]. If the noise distribution is only assumed to be separable across measurements, we can use a splitting loss

$$\mathcal{L}_{\text{SPLIT}}(\theta, \mathbf{y}_i) = \mathbb{E}_M \|(I - M)(A_i \text{R}_\theta(M\mathbf{y}_i, MA_i) - \mathbf{y}_i)\|_2^2$$

where  $M$  is a splitting mask sampled from a Bernoulli random variable or using problem-specific strategies (e.g. Neighbor2Neighbor [23], SSDU [62], etc.).

**Learning in the nullspace** If the finetuning dataset is associated with a single operator  $A_i = A$  for all  $i = 1, \dots, N$ , we choose  $\mathcal{L}_{\text{NULL}}$  as the Equivariant Imaging (EI) loss [11] which enforces equivariance to a group of transformations  $\{T_r\}_{r \in \mathcal{R}}$  such as rotations or shifts with

$$\mathcal{L}_{\text{EI}}(\theta) = \mathbb{E}_{r \sim \mathcal{R}} \|T_r \hat{\mathbf{x}}_{i,\theta} - \text{R}_\theta(AT_r \hat{\mathbf{x}}_{i,\theta}, A)\|_2^2$$

where  $\hat{\mathbf{x}}_{i,\theta} = \text{R}_\theta(\mathbf{y}_i, A_i)$  is the reconstructed image. If the finetuning dataset is associated with multiple operators  $\{A_r\}_{r \in \mathcal{R}}$ , we choose  $\mathcal{L}_{\text{NULL}}$  as the Multi Operator Imaging (MOI) loss [55], i.e.

$$\mathcal{L}_{\text{MOI}}(\theta) = \mathbb{E}_{r \sim \mathcal{R}} \|A_r \hat{\mathbf{x}}_{i,\theta} - \text{R}_\theta(A_r \hat{\mathbf{x}}_{i,\theta}, A_r)\|_2^2$$

also where  $\hat{\mathbf{x}}_{i,\theta} = \text{R}_\theta(\mathbf{y}_i, A_i)$ , which enforces consistency across operators  $A_i \hat{\mathbf{x}} \approx A_r \hat{\mathbf{x}}$  for all pairs  $(i, r)$ .

## 5. Results

### 5.1. Baselines

We evaluate our model’s performance alongside both iterative reconstruction methods, unrolled models and end-to-end architectures. First, we consider the Plug-and-Play model DPIR [68], which plugs a DRUNet, trained only for denoising, within an 8-step Half Quadratic Splitting (HQS) algorithm [2], thereby requiring approximately eight times as many FLOPs as our model (see Tab. 3 for detail). We also compare with unrolled versions of DPIR (referred to as uDPIR), also comprising eight HQS iterations, that we train on the same tasks, with the same loss function and dataset as our model. Specifically, we investigate both the weight-tied variant, where all eight iterations share the same DRUNet parameters, and the weight-untied variant, where each iteration has its own set of parameters—resulting in a model with eight times more parameters than

<sup>2</sup>In this section we do not explicit the dependency of  $\text{R}_\theta$  on  $(\sigma, \gamma)$ .

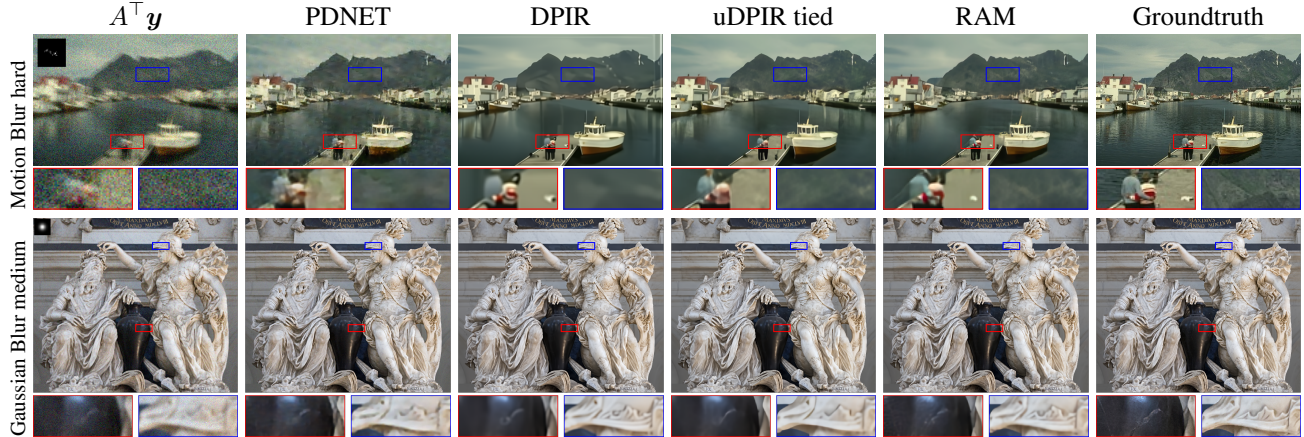


Figure 4. **Deblurring results.** Top row: motion blur hard, on a CBS68 sample. Bottom row: Gaussian blur medium, on a Div2k sample.

Method	MRI $\times 4$		MRI $\times 8$		CT	
	PSNR	SSIM	PSNR	SSIM	PSNR	SSIM
PDNet	28.25	0.719	24.54	0.641	23.09	0.713
DPIR	30.54	0.784	25.28	0.661	n.a.	n.a.
uDPIR-untied	33.73	0.848	30.20	0.792	27.00	0.772
uDPIR-tied	34.14	0.851	30.86	0.805	28.35	0.779
RAM	34.39	0.853	31.50	0.813	28.83	0.798

Table 2. **Reconstruction metrics for different methods on MRI and CT problems.** Left and middle: single-coil MRI with factors 4 and 8, respectively. Right: computed tomography.

	PDNet	uDPIR-untied	uDPIR-tied	RAM
GFLOPS	60	2234	2234	360
Test memory (BS=1)	52	1213	298	354
Train memory (BS=8)	5815	37288	36374	9670

Table 3. **Computational metrics.** Floating point operations (FLOPs) and memory requirements in MBytes for different methods on  $256 \times 256$  color image motion deblurring.

RAM. Additionally, we compare our approach with the PDNet unrolled network [1], trained on the same tasks. Finally, we evaluate Restormer [63], a transformer-based model with a similar computational cost (in terms of FLOPs) to DRUNet, but trained separately on each restoration tasks.

## 5.2. In-distribution results

We first evaluate the proposed method on tasks that are consistent with the training tasks.

**Deblurring** In this case, the inverse problem is  $\mathbf{y} = \mathbf{k} * \mathbf{x} + \sigma \mathbf{n}$ , where  $\mathbf{k}$  is some blur kernel and  $\mathbf{n} \sim \mathcal{N}(\mathbf{0}, I)$ . We show in Table 1 results on the motion and Gaussian denoising tasks. For each case, we establish 3 types of problems (easy, medium and hard) corresponding to different kernel lengths and noise standard deviations. **Motion deblurring:** we generate random motion blur problems as per [52, 57] with psf size of 31; the difficulty of the problem is defined by the length scale of blur trajectories  $\ell$ , the standard deviation of the Gaussian processes  $s$  generating the psf and the standard deviation  $\sigma$  of the additive Gaussian noise. The tuple  $\{\ell, s, \sigma\}$  are set to  $\{0.1, 0.1, 0.01\}$ ,  $\{0.6, 0.5, 0.05\}$ ,  $\{1.2, 1.0, 0.1\}$  for the easy, medium and hard settings respectively. **Gaussian deblurring:** we generate fixed blur kernels with psf of size 31; the difficulty of the problem is defined by the standard deviation of the blur kernel  $\sigma_{\text{blur}}$  and the standard deviation  $\sigma$  of the additive Gaussian noise. The tuple  $\{\sigma_{\text{blur}}, \sigma\}$  is set to  $\{1.0, 0.01\}$ ,  $\{2.0, 0.05\}$ ,  $\{4.0, 0.1\}$  for the easy, medium and hard settings respectively. Visual results are proposed in Fig. 4 with associated metrics in Tab. 3. We observe that the best performing methods are the proposed RAM and uDPIR-tied. Surprisingly, we observe that uDPIR-untied underperforms compared to its tied counterpart, despite having significantly more parameters. The proposed model generally outperforms other methods, except in motion deblurring on the Urban100 dataset. In this case, the operator  $A$  being nearly invertible, we hypothesize that proximal steps with strong regularization parameters in the DPIR algorithm help mitigate the mild bias introduced by the large image size, which differs from the training patch sizes.

**MRI** We consider the validation set of the fastMRI brain dataset and apply the single-coil accelerated acquisition procedure from [65], with acceleration factors 4 and 8. In this context, the problem writes  $\mathbf{y} = M\mathbf{F}\mathbf{x} + \sigma \mathbf{n}$ , where  $M$  is a binary mask

and  $F$  is the discrete Fourier transform. We add Gaussian random noise with standard deviation  $\sigma = 5 \cdot 10^{-4}$ . Reconstruction metrics are provided in Table 2, along with visuals in Figure 5. The proposed RAM model outperforms other methods. Interestingly, we notice that PDNet struggles on this task. This is the consequence of the learning in the measurement domain that varies greatly from one inverse problem to another, making the multitask learning harder.

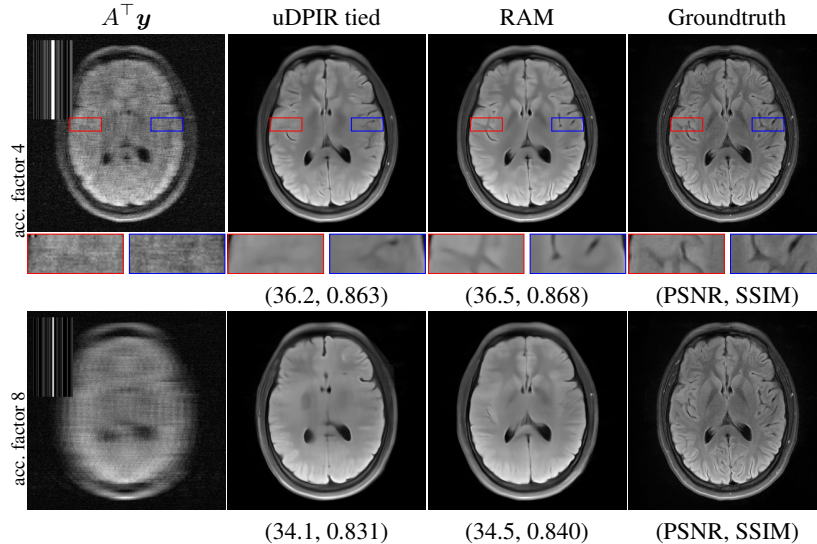


Figure 5. Results on MRI for acceleration factors 4 and 8. The Fourier mask is shown in the top left corner of the backprojection.

**Computed Tomography** We consider the computed tomography problem with Gaussian additive noise, writing  $y = Ax + \sigma n$ , where  $A$  is the Radon transform and  $n \sim \mathcal{N}(\mathbf{0}, I)$ . We consider an acquisition with 51 angles, corresponding to approximately 10% of the width of images in the LIDC-IDRI dataset. Similarly to the training setup, we fix  $\sigma = 10^{-4}$ . Numerical results are provided in the rightmost column of Table 2. We do not report values for the DPIR algorithm as we did not manage to obtain meaningful results for this particular problem. As observed in Figure 6, we observe that the proposed RAM model yields images with more details than uDPIR-tied.

### 5.3. Out-of distribution performance

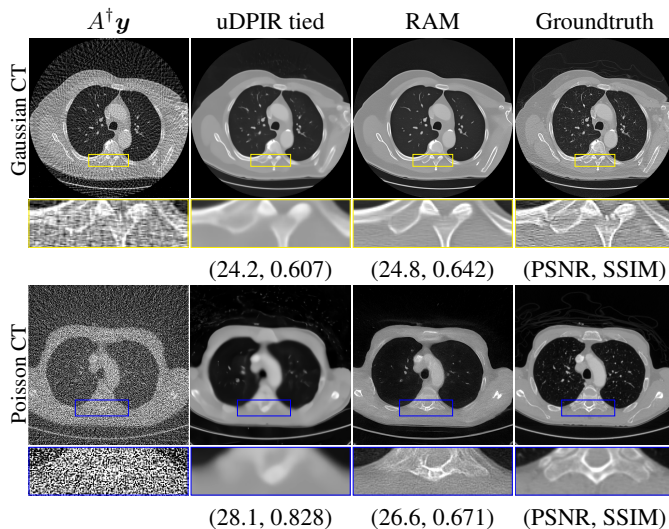


Figure 6. Results on CT. Top row: CT with Gaussian noise, similar to the training setup. Bottom row: CT with Poisson noise, unseen during training.

Method	mcMRI $\times 8$		Poisson CT	
	PSNR	SSIM	PSNR	SSIM
PDNet	n.a.	n.a.	13.20	0.357
UNet [65]	28.50	0.662	n.a.	n.a.
uDPIR-untied	33.71	0.850	14.62	0.446
uDPIR-tied	36.06	0.894	14.67	0.462
RAM	35.62	0.889	28.83	0.798

Table 4. Performance metrics on MRI and CT problems. Left column: multi-coil MRI with acceleration factors 8. Right column: computed tomography with Poisson noise.



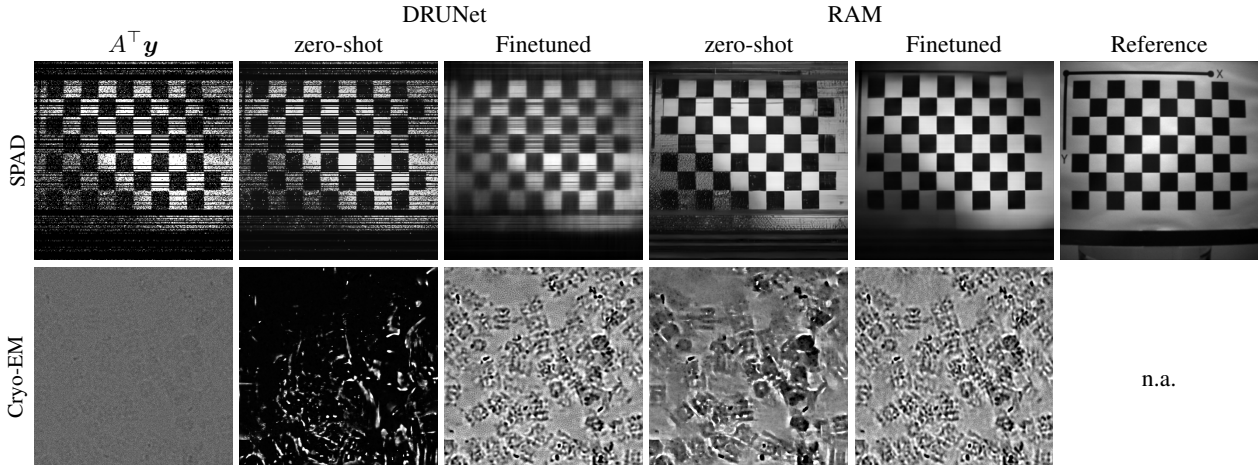


Figure 7. **Finetuning on real data with complex noise.** RAM can be finetuned on a few real LinoSPAD or Cryo-EM images without ground-truth nor full knowledge of the noise distribution.

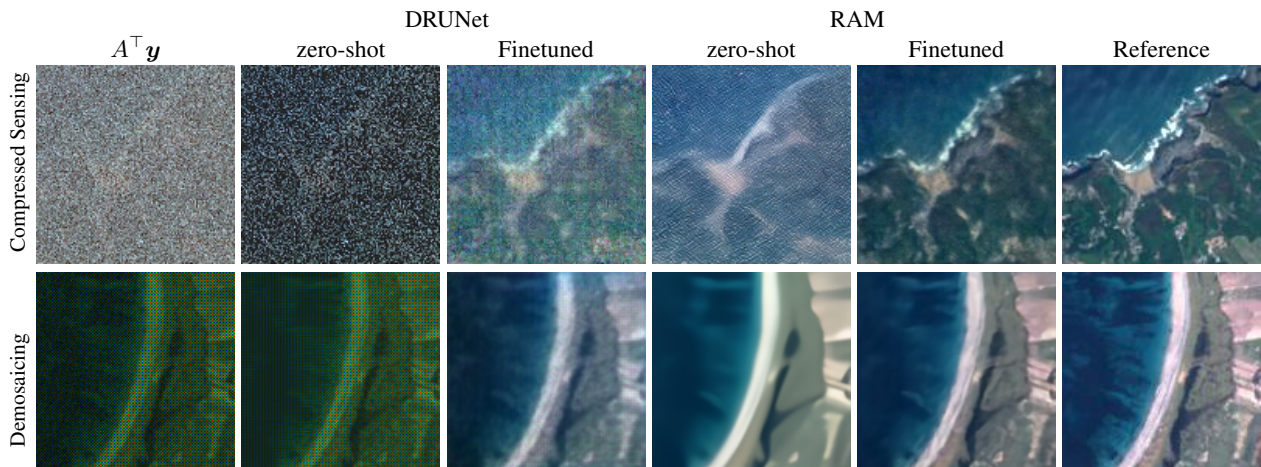


Figure 8. **Self-supervised finetuning with a single image.** Adaptation to new problems (compressed sensing and demosaicing) and new distributions (Sentinel 2 images), by finetuning on measurements of a single image.

**Multi-coil MRI** We consider the Cartesian multi-coil MRI problem. In this setup, and assuming  $L$  coils, the signal measured by each coil  $\ell \in \{1, \dots, L\}$  writes as  $\mathbf{y}_\ell = MFS_\ell \mathbf{x} + \sigma \mathbf{n}_\ell$ , where the  $(S_\ell)_{1 \leq \ell \leq L}$  are the sensitivity maps (or S-maps). We provide reconstruction metrics for the multi-coil setting in Tab. 2 and associated visuals in Fig. 6. We provide comparisons with the baseline UNet from [65]. Both methods perform similarly up to the addition of mild residual noise with the UNet, yielding lower PSNR despite similar visual results. We stress that since PDNet contains learnable layers acting in the measurement domain, one would need to retrain the architecture for this new setting specifically, hence we do not present the results.

**Computed Tomography with Poisson noise** While our model was trained on the CT problem with Gaussian noise, we propose to apply it to a CT problem degraded with Poisson noise. In this setting, the problem writes  $\mathbf{y} = \gamma \mathcal{P}(A\mathbf{x}/\gamma)$ , where  $\gamma > 0$  represents the gain of Poisson noise, while  $A$  is the sparse Radon transform. As previously, we consider a problem with 51 angles. Numerical results are provided in Tab. 4 and visual results in Fig. 6. Notice the the proposed methods performs better at estimating the texture in the scanner.

## 5.4. Finetuning results

We assess the proposed model on various imaging tasks and data that were not seen during training. Our results demonstrate that finetuning RAM with a minimal number of training images (as few as a single image) significantly enhances its perfor-

Model	Compressed Sensing						Demosaicing					
	DRUNet rand		DRUNet		RAM		DRUNet rand		DRUNet		RAM	
	Sup.	Self.	Sup.	Self.	Sup.	Self.	Sup.	Self.	Sup.	Self.	Sup.	Self.
zero-shot	8.07		10.23		22.50		8.10		10.73		29.49	
$N = 1$	20.92	21.20	19.49	19.44	30.77	30.40	23.14	21.28	25.82	25.57	34.46	33.89
$N = 10$	22.59	22.00	25.99	24.74	32.52	32.29	24.85	21.85	33.14	31.38	35.03	34.73
$N = 100$	22.73	22.24	28.38	30.58	33.40	33.57	25.84	23.22	34.06	34.56	35.26	35.10

Table 6. **Effect of finetuning dataset size and self-supervision.** RAM requires few observations to obtain good results, whereas finetuning a DRUNet denoiser requires larger datasets.

mance. This finetuning process requires only a few minutes on a single GPU, and enables RAM to effectively tackle any image inverse problems, even in the absence of training data. For comparison, we also finetune both pretrained and randomly initialized (untrained) DRUNet baselines.

**Satellite images** We use a dataset of 200 images of  $128 \times 128$  pixels of the coast of the United Kingdom taken by the Sentinel-2 L1C satellite with 10-meter resolution and minimal cloud coverage, keeping only the bands corresponding to red, green, and blue. The dataset is split into 100 images for training and 100 for testing. **Compressed sensing:** we set  $A = SM$  where  $M$  is a random mask with values in  $\{-1, +1\}$ , and  $S \in \mathbb{R}^{m \times n}$  is the discrete sine transform with output randomly subsampled by a factor of 4. **Demosaicing:** measurements are generated by applying a Bayer pattern, keeping a single band per pixel. In both cases, we consider Gaussian noise with  $\sigma = 0.05$ , and finetune with the  $\ell_2$  loss for the supervised case, and with  $\mathcal{L}_{\text{SURE}}$  and  $\mathcal{L}_{\text{EI}}$  (using shifts) for the self-supervised setting. As shown in Table 6 and Figure 8, finetuning RAM requires only on a *single image* to obtain good results, significantly outperforming the DRUNet baselines. As shown in Table 5, self-supervised finetuning can be performed in the order of a couple of minutes on a single mid-sized GPU.

**Cryo electron microscopy** We evaluate the model on 5 real Cryo-EM images of  $7676 \times 7420$  pixels provided by the Topaz-EM open-source library [8] whose noise distribution is unknown and have very low SNR. We finetune our model of  $256 \times 256$  crops using  $\mathcal{L}_{\text{SPLIT}}$  to handle the unknown noise distribution. Reconstructions are shown in Figure 7.

**Low-photon imaging** We evaluate the RAM model on the LinoSPAD data provided by Lindell et al. [33], which is corrupted by photon noise. While noise in SPADs is generally assumed to be Poisson in the very low-flux case, images acquired with higher flux can follow more complex discrete noise distributions. The LinoSPAD scans the image using epipolar scanning, with some lines of pixels removed due to faulty acquisition. Thus, the image recovery problem in this case is inpainting. The missing line pattern and noise model were not used during model training. We finetune the model using  $\mathcal{L}_{\text{SPLIT}}$  and  $\mathcal{L}_{\text{MOI}}$  (removing random subsets of lines). Reconstructions are shown in Figure 7.

## 6. Discussion

In this work, we show that it is possible to obtain competitive reconstruction performance without following the common practice of unrolling an optimization algorithm, which results in a faster and lighter reconstruction network.

Moreover, we challenge the idea that a reconstruction network has to be specialized to a specific imaging task and show that it is possible to obtain good reconstructions across a wide variety of tasks and imaging modalities with a relatively lightweight network of the size of the standard DRUNet denoiser. Our results suggest that imaging tasks that might seem very different (Cryo-EM denoising and demosaicing of satellite images) share a significant common structure and can be tackled with the same model. Nevertheless, we believe that this work raises the question of whether bigger networks that leverage well-designed measurement conditioning can obtain even better performances.

**Limitations** Training the RAM model requires a fair amount of GPU resources, which might not be available to all practitioners. Nevertheless, our model can be finetuned on a single mid-sized GPU, obtaining competitive results with a few

	Compressed Sensing	Demosaicing
$N = 1$	43	60
$N = 10$	80	107
$N = 100$	228	267

Table 5. **Self-supervised finetuning time in seconds.** Results for the finetuning experiments on the Sentinel 2 data. An NVIDIA RTX 4090 GPU was used for the finetuning experiments.

optimization steps on small finetuning datasets. We focus on low-distortion reconstructions, in contrast to the higher perceptual quality and higher distortion of diffusion methods [10]. However, reconstructors such as RAM can be used within sampling algorithms, e.g. [14, 41].

## 7. Conclusion

We present a new lightweight foundational model for computational imaging that obtains state-of-the-art performance on a wide range of problems, outperforming PnP methods while providing similar results to  $8\times$  more compute-intensive unrolled networks. Moreover, our model displays transfer capabilities, as it can be finetuned on new datasets or imaging problems with small datasets (up to a single image) in a fully self-supervised way, i.e. without any ground-truth references. We believe this work paves the way for a new approach to imaging, where most of the effort can be put into developing strong base models and robust self-supervised finetuning techniques.

## References

- [1] Jonas Adler and Ozan Öktem. Learned primal-dual reconstruction. *IEEE transactions on medical imaging*, 37(6):1322–1332, 2018. [2](#), [3](#), [7](#)
- [2] Hemant K. Aggarwal, Merry P. Mani, and Mathews Jacob. MoDL: Model-Based Deep Learning Architecture for Inverse Problems. *IEEE Transactions on Medical Imaging*, 38(2):394–405, 2019. [6](#)
- [3] Amir Aghabiglou, Matthieu Terris, Adrian Jackson, and Yves Wiaux. Deep network series for large-scale high-dynamic range imaging. In *ICASSP 2023-2023 IEEE International Conference on Acoustics, Speech and Signal Processing (ICASSP)*, pages 1–5. IEEE, 2023. [3](#)
- [4] Eirikur Agustsson and Radu Timofte. Ntire 2017 challenge on single image super-resolution: Dataset and study. In *The IEEE Conference on Computer Vision and Pattern Recognition (CVPR) Workshops*, 2017. [6](#)
- [5] Samuel G Armato III, Geoffrey McLennan, Luc Bidaut, Michael F McNitt-Gray, Charles R Meyer, Anthony P Reeves, Binsheng Zhao, Denise R Aberle, Claudia I Henschke, Eric A Hoffman, et al. The lung image database consortium (lidc) and image database resource initiative (idri): a completed reference database of lung nodules on ct scans. *Medical physics*, 38(2):915–931, 2011. [5](#), [14](#)
- [6] Joshua Batson and Loic Royer. Noise2Self: Blind Denoising by Self-Supervision. In *Proceedings of the 36th International Conference on Machine Learning*. PMLR, 2019. [4](#)
- [7] Chinmay Belthangady and Loic A. Royer. Applications, Promises, and Pitfalls of Deep Learning for Fluorescence Image Reconstruction. *Nature Methods*, 16:1215–1225, 2019. [2](#), [3](#), [5](#)
- [8] Tristan Bepler, Kotaro Kelley, Alex J. Noble, and Bonnie Berger. Topaz-Denoise: general deep denoising models for cryoEM and cryoET. *Nature Communications*, 11(1):5208, 2020. [10](#)
- [9] Carla Bertocchi, Emilie Chouzenoux, Marie-Caroline Corbineau, Jean-Christophe Pesquet, and Marco Prato. Deep unfolding of a proximal interior point method for image restoration. *Inverse Problems*, 36(3):034005, 2020. [3](#)
- [10] Yochai Blau and Tomer Michaeli. The perception-distortion tradeoff. In *Proceedings of the IEEE Conference on Computer Vision and Pattern Recognition (CVPR)*, pages 6228–6237, 2018. [2](#), [11](#)
- [11] Dongdong Chen, Julián Tachella, and Mike E. Davies. Equivariant Imaging: Learning Beyond the Range Space. In *Proceedings of the IEEE/CVF Conference on Computer Vision and Pattern Recognition*, pages 4379–4388, 2021. [4](#), [5](#), [6](#)
- [12] Hyungjin Chung, Byeongsu Sim, Dohoon Ryu, and Jong Chul Ye. Improving diffusion models for inverse problems using manifold constraints. *Advances in Neural Information Processing Systems*, 35:25683–25696, 2022. [2](#), [3](#)
- [13] Giannis Daras, Hyungjin Chung, Chieh-Hsin Lai, Yuki Mitsufuji, Jong Chul Ye, Peyman Milanfar, Alexandros G Dimakis, and Mauricio Delbracio. A survey on diffusion models for inverse problems. *arXiv preprint arXiv:2410.00083*, 2024. [2](#), [3](#)
- [14] Mauricio Delbracio and Peyman Milanfar. Inversion by direct iteration: An alternative to denoising diffusion for image restoration. *Transactions on Machine Learning Research*, 2023. Featured Certification. [11](#)
- [15] Cihat Eldeniz, Weijie Gan, Sihao Chen, Tyler J. Fraum, Daniel R. Ludwig, Yan Yan, Jiaming Liu, Thomas Vahle, Uday Krishnamurthy, Ulugbek S. Kamilov, and Hongyu An. Phase2Phase: Respiratory Motion-Resolved Reconstruction of Free-Breathing Magnetic Resonance Imaging Using Deep Learning Without a Ground Truth for Improved Liver Imaging. *Investigative Radiology*, 56(12):809, 2021. [5](#)
- [16] Hang Guo, Jinmin Li, Tao Dai, Zhihao Ouyang, Xudong Ren, and Shu-Tao Xia. Mambair: A simple baseline for image restoration with state-space model. In *European conference on computer vision*, pages 222–241. Springer, 2024. [3](#)
- [17] Wolfgang Hackbusch. *Multi-grid methods and applications*. Springer Science & Business Media, 2013. [4](#)
- [18] Kerstin Hammernik, Teresa Klatzer, Erich Kobler, Michael P Recht, Daniel K Sodickson, Thomas Pock, and Florian Knoll. Learning a variational network for reconstruction of accelerated mri data. *Magnetic resonance in medicine*, 79(6):3055–3071, 2018. [2](#), [3](#)
- [19] Allard A. Hendriksen, Daniel M. Pelt, and K. Joost Batenburg. Noise2Inverse: Self-supervised deep convolutional denoising for tomography. *IEEE Transactions on Computational Imaging*, 6:1320–1335, 2020. [5](#)

- [20] Sébastien Herbretreau, Emmanuel Moebel, and Charles Kervrann. Normalization-equivariant neural networks with application to image denoising. In *Advances in Neural Information Processing Systems*, pages 5706–5728, 2023. 3
- [21] Johannes Hertrich, Sebastian Neumayer, and Gabriele Steidl. Convolutional proximal neural networks and plug-and-play algorithms. *Linear Algebra and its Applications*, 631:203–234, 2021. 2
- [22] Jia-Bin Huang, Abhishek Singh, and Narendra Ahuja. Single image super-resolution from transformed self-exemplars. In *CVPR*, 2015. 6
- [23] Tao Huang, Songjiang Li, Xu Jia, Huchuan Lu, and Jianzhuang Liu. Neighbor2Neighbor: Self-Supervised Denoising from Single Noisy Images. In *2021 IEEE/CVF Conference on Computer Vision and Pattern Recognition (CVPR)*, pages 14776–14785, Nashville, TN, USA, 2021. IEEE. 5, 6
- [24] Samuel Hurault, Arthur Leclaire, and Nicolas Papadakis. Gradient step denoiser for convergent plug-and-play. *arXiv preprint arXiv:2110.03220*, 2021. 2
- [25] Kyong Hwan Jin, Michael T McCann, Emmanuel Froustey, and Michael Unser. Deep convolutional neural network for inverse problems in imaging. *IEEE transactions on image processing*, 26(9):4509–4522, 2017. 3
- [26] J Kaiser and R Schafer. On the use of the  $i_0$ -sinh window for spectrum analysis. *IEEE Transactions on Acoustics, Speech, and Signal Processing*, 28(1):105–107, 1980. 4
- [27] Tero Karras, Miika Aittala, Timo Aila, and Samuli Laine. Elucidating the design space of diffusion-based generative models. *Advances in neural information processing systems*, 35:26565–26577, 2022. 3
- [28] Tero Karras, Miika Aittala, Jaakko Lehtinen, Janne Hellsten, Timo Aila, and Samuli Laine. Analyzing and improving the training dynamics of diffusion models. In *Proceedings of the IEEE/CVF Conference on Computer Vision and Pattern Recognition*, pages 24174–24184, 2024. 3
- [29] Guillaume Lauga, Elisa Riccietti, Nelly Pustelnik, and Paulo Gonçalves. Iml fista: A multilevel framework for inexact and inertial forward-backward. application to image restoration. *SIAM Journal on Imaging Sciences*, 17(3):1347–1376, 2024. 4
- [30] Robert Michael Lewis and Stephen G. Nash. Model Problems for the Multigrid Optimization of Systems Governed by Differential Equations. *SIAM Journal on Scientific Computing*, 26(6):1811–1837, 2005. Publisher: Society for Industrial and Applied Mathematics. 4
- [31] Yawei Li, Kai Zhang, Jingyun Liang, Jiezhang Cao, Ce Liu, Rui Gong, Yulun Zhang, Hao Tang, Yun Liu, Denis Demandolx, Rakesh Ranjan, Radu Timofte, and Luc Van Gool. Lsdnr: A large scale dataset for image restoration. In *Proceedings of the IEEE/CVF Conference on Computer Vision and Pattern Recognition*, pages 1775–1787, 2023. 5
- [32] Jingyun Liang, Jiezhang Cao, Guolei Sun, Kai Zhang, Luc Van Gool, and Radu Timofte. SwinIR: Image restoration using swin transformer. In *ICCV Workshops*, 2021. 3
- [33] David B. Lindell, Matthew O’Toole, and Gordon Wetzstein. Single-Photon 3D Imaging with Deep Sensor Fusion. *ACM Trans. Graph. (SIGGRAPH)*, (4), 2018. 10
- [34] Ziwei Luo, Fredrik K. Gustafsson, Zheng Zhao, Jens Sjölund, and Thomas B. Schön. Controlling vision-language models for multi-task image restoration. In *The Twelfth International Conference on Learning Representations*, 2024. 3
- [35] Stéphane Mallat. *A Wavelet Tour of Signal Processing, The Sparse Way*. Academic Press, Elsevier, 3rd edition edition, 2009. 2
- [36] David Martin, Charless Fowlkes, Doron Tal, and Jitendra Malik. A database of human segmented natural images and its application to evaluating segmentation algorithms and measuring ecological statistics. In *ICCV*, 2001. 6
- [37] Peyman Milanfar and Mauricio Delbracio. Denoising: A powerful building-block for imaging, inverse problems, and machine learning. *arXiv preprint arXiv:2409.06219*, 2024. 2
- [38] Sreyas Mohan, Zahra Kadkhodaie, Eero P. Simoncelli, and Carlos Fernandez-Granda. Robust and interpretable blind image denoising via bias-free convolutional neural networks. In *International Conference on Learning Representations*, 2020. 3, 5
- [39] Brayan Monroy, Jorge Bacca, and Julián Tachella. Generalized Recorruped-to-Recorruped: Self-Supervised Learning Beyond Gaussian Noise. In *2025 IEEE/CVF Conference on Computer Vision and Pattern Recognition (CVPR)*, Nashville, TN, USA, 2025. IEEE. 6
- [40] Jorge Nocedal and Stephen J Wright. *Numerical optimization*. Springer, 1999. 4
- [41] Guy Ohayon, Tomer Michaeli, and Michael Elad. Posterior-mean rectified flow: Towards minimum MSE photo-realistic image restoration. In *The Thirteenth International Conference on Learning Representations*, 2025. 11
- [42] Jean-Christophe Pesquet, Audrey Repetti, Matthieu Terris, and Yves Wiaux. Learning maximally monotone operators for image recovery. *SIAM Journal on Imaging Sciences*, 14(3):1206–1237, 2021. 2
- [43] Sathish Ramani, Thierry Blu, and Michael Unser. Monte-Carlo Sure: A Black-Box Optimization of Regularization Parameters for General Denoising Algorithms. *IEEE Transactions on Image Processing*, 17(9):1540–1554, 2008. 6
- [44] Zaccharie Ramzi, GR Chaithya, Jean-Luc Starck, and Philippe Ciuciu. Nc-pdnet: A density-compensated unrolled network for 2d and 3d non-cartesian mri reconstruction. *IEEE Transactions on Medical Imaging*, 41(7):1625–1638, 2022. 2, 3
- [45] Edward T Reehorst and Philip Schniter. Regularization by denoising: Clarifications and new interpretations. *IEEE transactions on computational imaging*, 5(1):52–67, 2018. 3
- [46] Yaniv Romano, Michael Elad, and Peyman Milanfar. The little engine that could: Regularization by denoising (red). *SIAM Journal on Imaging Sciences*, 10(4):1804–1844, 2017. 3

- [47] Robin Rombach, Andreas Blattmann, Dominik Lorenz, Patrick Esser, and Björn Ommer. High-resolution image synthesis with latent diffusion models. In *Proceedings of the IEEE/CVF conference on computer vision and pattern recognition*, pages 10684–10695, 2022. 3
- [48] Olaf Ronneberger, Philipp Fischer, and Thomas Brox. U-net: Convolutional networks for biomedical image segmentation. In *Medical image computing and computer-assisted intervention—MICCAI 2015: 18th international conference, Munich, Germany, October 5–9, 2015, proceedings, part III 18*, pages 234–241. Springer, 2015. 3
- [49] Leonid I Rudin, Stanley Osher, and Emad Fatemi. Nonlinear total variation based noise removal algorithms. *Phys. D*, 60:259–268, 1992. 2
- [50] Chitwan Saharia, William Chan, Saurabh Saxena, Lala Li, Jay Whang, Emily L Denton, Kamyar Ghasemipour, Raphael Gontijo Lopes, Burcu Karagol Ayan, Tim Salimans, et al. Photorealistic text-to-image diffusion models with deep language understanding. *Advances in neural information processing systems*, 35:36479–36494, 2022. 3
- [51] Yash Sanghvi, Abhiram Gnanasambandam, and Stanley H Chan. Photon limited non-blind deblurring using algorithm unrolling. *IEEE Transactions on Computational Imaging*, 8:851–864, 2022. 3
- [52] Christian J Schuler, Michael Hirsch, Stefan Harmeling, and Bernhard Schölkopf. Learning to deblur. *IEEE transactions on pattern analysis and machine intelligence*, 38(7):1439–1451, 2015. 7
- [53] Yang Song and Stefano Ermon. Generative modeling by estimating gradients of the data distribution. *Advances in neural information processing systems*, 32, 2019. 3
- [54] Charles M. Stein. Estimation of the Mean of a Multivariate Normal Distribution. 9(6):1135–1151, 1981. 6
- [55] Julián Tachella, Dongdong Chen, and Mike Davies. Unsupervised Learning From Incomplete Measurements for Inverse Problems. *Advances in Neural Information Processing Systems*, 35:4983–4995, 2022. 5, 6
- [56] Julian Tachella, Dongdong Chen, and Mike Davies. Sensing Theorems for Unsupervised Learning in Linear Inverse Problems. *Journal of Machine Learning Research (JMLR)*, 2023. 4, 6
- [57] J Tachella, D Chen, S Hurault, M Terris, and A Wang. Deepinverse: A deep learning framework for inverse problems in imaging. URL: <https://deepinv.github.io/deepinv>, 2023. 5, 7
- [58] Julián Tachella, Mike Davies, and Laurent Jacques. UNSURE: Self-supervised learning with Unknown Noise level and Stein’s Unbiased Risk Estimate. In *The Thirteenth International Conference on Learning Representations*, 2024. 5, 6
- [59] Matthieu Terris, Thomas Moreau, Nelly Pustelnik, and Julian Tachella. Equivariant plug-and-play image reconstruction. In *Proceedings of the IEEE/CVF Conference on Computer Vision and Pattern Recognition*, pages 25255–25264, 2024. 2
- [60] Singanallur V Venkatakrishnan, Charles A Bouman, and Brendt Wohlberg. Plug-and-play priors for model based reconstruction. In *2013 IEEE global conference on signal and information processing*, pages 945–948. IEEE, 2013. 2, 3
- [61] Pascal Vincent. A connection between score matching and denoising autoencoders. *Neural computation*, 23(7):1661–1674, 2011. 3
- [62] Burhaneddin Yaman, Seyed Amir Hossein Hosseini, Steen Moeller, Jutta Ellermann, Kâmil Uğurbil, and Mehmet Akçakaya. Self-Supervised Physics-Based Deep Learning MRI Reconstruction Without Fully-Sampled Data. In *2020 IEEE 17th International Symposium on Biomedical Imaging (ISBI)*, pages 921–925, 2020. 4, 6
- [63] Syed Waqas Zamir, Aditya Arora, Salman Khan, Munawar Hayat, Fahad Shahbaz Khan, and Ming-Hsuan Yang. Restormer: Efficient transformer for high-resolution image restoration. In *CVPR*, 2022. 7
- [64] Syed Waqas Zamir, Aditya Arora, Salman Khan, Munawar Hayat, Fahad Shahbaz Khan, and Ming-Hsuan Yang. Restormer: Efficient transformer for high-resolution image restoration. In *Proceedings of the IEEE/CVF conference on computer vision and pattern recognition*, pages 5728–5739, 2022. 3
- [65] Jure Zbontar, Florian Knoll, Anuroop Sriram, Tullie Murrell, Zhengnan Huang, Matthew J Muckley, Aaron Defazio, Ruben Stern, Patricia Johnson, Mary Bruno, et al. fastmri: An open dataset and benchmarks for accelerated mri. *arXiv preprint arXiv:1811.08839*, 2018. 3, 5, 7, 8, 9, 14, 15
- [66] Kai Zhang, Wangmeng Zuo, Yunjin Chen, Deyu Meng, and Lei Zhang. Beyond a gaussian denoiser: Residual learning of deep CNN for image denoising. *TIP*, 2017. 3
- [67] Kai Zhang, Wangmeng Zuo, Shuhang Gu, and Lei Zhang. Learning deep cnn denoiser prior for image restoration. In *Proceedings of the IEEE conference on computer vision and pattern recognition*, pages 3929–3938, 2017. 3
- [68] Kai Zhang, Luc Van Gool, and Radu Timofte. Deep unfolding network for image super-resolution. In *Proceedings of the IEEE/CVF conference on computer vision and pattern recognition*, pages 3217–3226, 2020. 3, 6
- [69] Kai Zhang, Yawei Li, Wangmeng Zuo, Lei Zhang, Luc Van Gool, and Radu Timofte. Plug-and-play image restoration with deep denoiser prior. *TPAMI*, 2021. 2, 3, 4, 5
- [70] Kai Zhang, Yawei Li, Jingyun Liang, Jiezhong Cao, Yulun Zhang, Hao Tang, Deng-Ping Fan, Radu Timofte, and Luc Van Gool. Practical blind image denoising via swin-conv-unet and data synthesis. *Machine Intelligence Research*, 20(6):822–836, 2023. 2, 3
- [71] Yulun Zhang, Yapeng Tian, Yu Kong, Bineng Zhong, and Yun Fu. Residual dense network for image super-resolution. In *Proceedings of the IEEE conference on computer vision and pattern recognition*, pages 2472–2481, 2018. 3
- [72] Hang Zhao, Orazio Gallo, Iuri Frosio, and Jan Kautz. Loss Functions for Image Restoration With Neural Networks. *IEEE Transactions on Computational Imaging*, 3(1):47–57, 2017. 5
- [73] Yuanzhi Zhu, Kai Zhang, Jingyun Liang, Jiezhong Cao, Bihan Wen, Radu Timofte, and Luc Van Gool. Denoising diffusion models for plug-and-play image restoration. In *IEEE Conference on Computer Vision and Pattern Recognition Workshops (NTIRE)*, 2023. 2

## A. Datasets

### A.1. MRI

We perform virtual coil-combination on the raw kspace data from the brain-multicoil fastMRI dataset [65]. We use the resulting 70748 complex images from the training set for training our model and the 21842 slices from the validation set are reserved for validation.

### A.2. LIDC-IDRI

We use the LIDC-IDRI dataset [5] as a basis for our computed tomography experiments. We normalize the scans in hounsfield units using the rescale slope and intercept provided in the Dicom files. Data is clipped in the lung window values [-1200, 800] and the rescaled in [0, 1].

## B. Training inverse problems

We consider the following training problems. In what follows,  $\sigma_{\max} = 0.2$ .

### B.1. Color images

On natural images color images, our datasets of inverse problems contain the following tasks.

**Gaussian Denoising** Noise model: Gaussian noise with  $\sigma \sim \mathcal{U}(0.001, \sigma_{\max})$ .  $A$ : Identity transformation.

**Poisson-Gaussian Noise** Noise model: Poisson noise combined with Gaussian noise, with  $\sigma \sim \mathcal{U}(0.001, \sigma_{\max})$ .  $A$ : Identity transformation.

**Deblurring** Noise model: Gaussian noise with  $\sigma = 0.05$ . Forward model:  $A = h * x$ , where  $h$  is a convolutional blur kernel. The blur operator consists of a mixture of: (i) Motion blur ( $31 \times 31$  kernel), (ii) Gaussian blur ( $31 \times 31$  kernel), (iii) Additional Gaussian noise  $\sigma \sim \mathcal{U}(0.001, \sigma_{\max})$ .

**Inpainting** Noise model: Poisson-Gaussian noise. Forward model:  $A$  is a random mask, where pixels are retained with a probability  $p \sim \mathcal{U}(0.3, 0.9)$ . Two masking strategies: (i) Blockwise Bernoulli mask, (ii) Pixelwise Bernoulli mask. Each mask is combined with Gaussian noise  $\sigma \sim \mathcal{U}(0.01, \sigma_{\max})$  and Poisson noise.

**Super-Resolution (SR)** Noise model: Gaussian noise with  $\sigma = 0.01$ . Forward model:  $A$  is either a bicubic downsampling operator or a bilinear downsampling operator. The downsampling factor is chosen at random for each batch between 2 and 4.

**Pansharpening** Noise model: Gaussian noise with  $\sigma = 0.1$ .  $A$ : Multispectral-to-panchromatic fusion using Brovey sharpening. The spectral response function (SRF) is set to a flat profile, with reduction operation as sum-pooling.

### B.2. Complex images

For complex images our datasets of inverse problems contain the following tasks:

**FastMRI - Undersampled MRI Reconstruction** Noise model: Gaussian noise with  $\sigma = 5 \times 10^{-4}$ . Forward model:  $A$  is an undersampled Fourier transform with a random mask at acceleration factors 4 or 8. Two acceleration settings: (i)  $A = MF$  with  $M \sim \mathcal{M}_4$  (acceleration 4), (ii)  $A = MF$  with  $M \sim \mathcal{M}_8$  (acceleration 8), where  $\mathcal{M}_r$  represents a Cartesian mask at acceleration factor  $r$  as in [65].

**FastMRI - Gaussian Denoising** Noise model: Gaussian noise with  $\sigma \sim \mathcal{U}(0.001, 0.1)$ . Forward model:  $A = I$  (Identity transformation).

**FastMRI - Inpainting** Noise model: Gaussian noise with  $\sigma = 0.1$ . Forward model:  $A$  is a binary mask with probability  $p \sim \mathcal{U}(0.1, 0.9)$ . Masking strategy: Bernoulli-distributed missing pixels with random mask density.

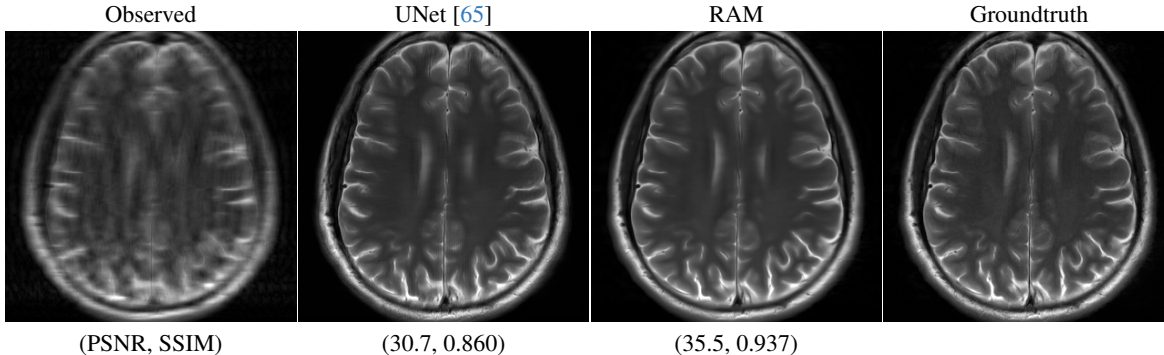


Figure 9. Results on the multi-coil MRI problem with acceleration factor 8.

### B.3. Single channel images

In the case of grayscale images, our inverse problems include all the ones used for color images. Additionally, we also consider CT scans.

**LIDC-IDRI - Tomographic Reconstruction** Noise model: Gaussian noise with  $\sigma = 0.01$ . Forward model:  $A$  is a Radon transform with 10 projection angles uniformly spaced in  $[0^\circ, 180^\circ]$ .

### C. Finetuning

In all finetuning experiments, we use the Adam optimizer with the same parameters used at train time (see Section 3.2). In all experiments and baselines, we pick the network checkpoint obtaining the best performance using ground truth for the Sentinel experiments, and visual inspection for the SPAD and Cryo-EM data. The trade-off parameter in (8) is set as  $\omega = 0.1$ . Shifts up to 10% of the image width and height are considered in the EI loss. Figure 8 shows reconstructions for a finetuning on a single measurement on both compressed sensing and demosaicing problems.

### D. Multi-coil MRI results

We provide in Fig. 9 results on the multicoil MRI inverse problem where we simulate  $L = 15$  coil maps. The UNet reconstruction shows a less smooth aspect, penalizing PSNR.